2

Silicon–Rich Silicon Oxide Thin Films Fabricated by Electro-Chemical Method

Pham Van Hoi, Do Thuy Chi, Bui Huy and Nguyen Thuy Van
Vietnam Academy of Science and Technology,
Vietnam

1. Introduction

Porous silicon (PS) has attracted increasing research interest in basic physics as well as applications since 1990 when Canham reported on the efficient visible photoluminescence (PL) of porous silicon (Canham, 1990). Structurally, PS consists of many pores and silicon residuals and usually can be described as a homogeneous mixture of silicon, air and, even silicon dioxide. Based on porosity, PS can be classified into three types: nano, meso- and macro-pores. In the case of PS nano-pores, the size of both the silicon residuals and the air voids (pores) can be in the range of few nanometers. The exciton Bohr radius in Si is around 4.3 nm, so that quantum confinement can occur and change the electronic structure of those silicon nanocrystals. On the other hand, because the value of porosity is directly linked to the effective index of refraction of the PS layer, this layer appears as an effective medium, where the refractive index has a tunable value between the index of refraction of bulk Si and that of the air (pores). Those changes in the electronic structure and refractive index of PS when compared with bulk Si make it fascinating as both a low-dimensional material and an optical one. The considerable and controllable changes in the electronic structure and refractive index of PS fabricated by electrochemical anodization make it a promising material for photonics in comparison with bulk silicon and/ or pure silica. Using the oxidation process in O2 environment at high temperature, the PS samples become silicon-rich silicon oxides (SRSO), which has high chemical instability and avoids the aging of the PS that is important condition for optical devices such as planar optical waveguides, optical interference filters, micro-cavities, etc (Bettotti et al., 2002). During the last decade, Erbium (Er)-doped silicon-rich silicon oxide has attracted much interest due to its big potential application in Si-based optoelectronic devices for telecom and optical sensors. The Er-ions implanted in SRSO materials produce light emission at around wavelength range of 1540 nm, which corresponds to minimum light absorption in silica-based glass fibers. In this regard, a lot of studies have been carried out to improve the luminescence efficiency of this material. Such studies have revealed that co-implantation of Er and O_2 induce a strong enhancement in the Er-ions related emission at range of 1540 nm. In first case, samples were prepared by co-implanting Si and Er into silica thin films or co-sputtering Si, Er_2O_3 and SiO_2 on the silicon substrate (Shin et al., 1995). In second case, samples were prepared by implanting Er-ions into SiO_2 films containing Si-nanocrystals (nc-Si) and/or by Er-ion electrochemical deposition on silicon-rich oxide (SRSO) layers. The room temperature luminescence emission at the range of 1540 nm from Er-electrochemically doped porous

silicon was first reported by Kimura T. et al in 1994 (Kimura et al., 1994) and then followed by some other authors. The strong luminescence emission around 1540nm-range of Er-doped SRSO layers at room temperature can be explained by energy transfer from excitons confined in the nc-Si to Er-ions and the evidence of energy transfer had been revealed in photo-luminescent excitation spectra in visible and infrared region when the exciting wavelength was not equalized to resonant absorption wavelength of Er-ions. Up to now, there are very few evidences of energy transfer given in the case of Er-electrochemically doped SRSO layers.

In this book chapter, we will discuss the electrochemical method for preparing SRSO based on PS layers and Er-doped SRSO thin films for waveguide, optical filter and micro-cavity. In concentrating on the controllable changes in the refractive index of PS, we would like to use SRSO as a material for photonic devices such as optical interference filters, micro-cavities, etc. As an optical material, we present the fabrication method and properties of planar optical waveguides, active optical waveguides and optical interference filters operated in the range of infrared wavelengths. The advantage of optical waveguide amplifier based on Erbium-doped SRSO is the efficient energy transfer from electron-hole pairs generated in the Si nanocrystals to their neighbor erbium ions, which decay by emitting light at 1540nm (Bui Huy et al., 2008). The excitation cross-section of Er-ions in Er-doped SRSO is strongly increased in comparison of this one in the Er-doped silica glasses, so that the pump efficiency in Er-doped SRSO waveguides can be very high. The effect of energy transfer in elaborated Er-doped SRSO waveguides has also been explored. In order to design and predict the properties of the optical interference filters and micro-cavity based on SRSO multilayer, a simulation program based on the Transfer Matrix Method (TMM) was set up and the possible causes the difference in reflectivity spectra from this simulation and that from elaborated filters and/or cavity have been also given (Bui Huy et al., 2011). The structure and optical properties of SRSO layers are characterized by FE-SEM (Hitachi S-4800), M-line spectroscopy (Metricon 2010/M) and luminescent measurement. The energy transfer effect between silicon nanocrystals and Er ions in the SRSO layers has been obtained from experiments.

With the above-mentioned aim in mind, this chapter consists of the following sections: Section 2 presents the electrochemical method for preparing PS samples, Section 3 shows SRSO bi-layers based on PS annealed in oxygen environment at high temperature as a passive and active waveguides, Section 4 shows PS and/or SRSO multilayer with periodical refractive index change as an optical filter, Section 5 presents PS and/or SRSO multilayer with DFB configuration as micro-cavity, and Section 6 gives conclusions.

2. Electrochemical method for making SRSO thin films

The porous silicon thin films were formed from silicon wafers by electrochemical etching in hydro-fluoric acid, without the necessity of any deposition process (Smith et al., 1992). During this anodization process a part of the silicon is dissolved and the remaining crystalline silicon forms a sponge-like structure with porosity between some tens percent up to more than 90%. The microstructure of the PS depends on the doping level of the silicon wafers: the use of low doped p-type substrates results in nanoporous silicon (with pore and crystallite size less than 2 nm) and the use of highly doped substrates in mesoporous silicon (size of 2-50 nm) (Herino et al., 1987). In the both cases the structures are much smaller than the wavelength of visible light and the materials appear as a homogenous, effective optical

medium. The effective refractive index of the porous silicon thin films is mainly determined by the porosity which can be varied by several anodization parameters. The most suitable way is changing the anodization current density, with high current densities resulting in high porosities and low refractive indices.

A porous silicon thin film consisting of void spaces in silicon is created as a result of the electrochemical dissolution process in hydrofluoric acid, which can be expressed as in Equation (Valance, 1997):

$$Si + 4HF + 2F^- + 2h^+ \rightarrow SiF_6^{2-} + H_2 + 2H^- \quad (1)$$

The mass transport of positive charge carriers (h^+) in the substrate and reactant fluorine ions (F^-) in the electrolyte are key components in the dissolution process. As described in the model by Lehmann and Gösele (Lehman & Gösele, 1991), dissolution begins when holes reach the silicon surface under anodic bias and enable a fluorine ion to replace a hydrogen atom bonded to silicon. Due to the polarizing influence of the bound fluorine ion, further reaction are initiated in which fluorine ions continue to bind to the silicon atom and hydrogen gas is formed. When all four silicon bonds are broken, the silicon atoms become soluble and leave behind an atomic size corrugation in the former atomically flat surface. Pore formation continues at the surface irregularity where the electric field is concentrated and holes are available. The interpore space is depleted of holes, inhibiting sidewall dissolution.

In general, the preparation process of Er-doped silicon-rich silicon oxide layers can be divided into 3 steps: making a porous silicon (PS) layer by anodic etching of a Si-crystalline wafer in a HF solution; Er-ion deposition on the PS layer in Er content solution; and using thermal annealing at high temperature in oxygen and/or inert gases to obtain SRSO materials. The PS sample preparation is carried out in two approaches: keeping the current and/or the potential at a constant value during the electrochemical deposition (ECD) process. The difference between these two methods is that in the constant potential ECD, an n-type Si-crystalline wafer is usually used without annealing steps while in the constant current ECD, p-type Si-wafers are used and need thermal annealing. In our work we used both ECD methods for making PS layers on n- and p-type Si-crystalline wafers.

2.1 Experimental procedure

In the electrochemical method for fabrication of porous silicon thin films, silicon wafer acts as the anode and is situated at the bottom of the Teflon cell. The silicon wafer was coated Au-thin film in back-side and contacted to HF-resistant metallic electrode in the form of the disk. This electrode disk enables a uniform contact on the whole area of silicon wafer. The electrolyte is a mixture of hydrofluoric acid and ethanol (C_2H_5OH) at different concentrations and poured into the Teflon cell. The platinum wire, which is also chemically resistant to HF, acts as the cathode. The shape of the cathode is critical to ensuring homogeneous samples, because it must promote a uniform electric field while allowing hydrogen bubbles formed during the anodization process to escape. The Teflon cylindrical tube with diameters of 10-15mm was placed between the upper and lower parts of the Teflon cell. Finally, a stainless steel ring and nuts are used to hold the cell together. We can use either current or voltage source for the anodization process. In our experiments, we used the electrochemical system Autolab PGS-30 as the electric current source, which can control the current with the nano-Amper range. Figure 1 presents the experimental setup for

making porous silicon thin films. The computer-controlled electric source used for the electrochemical process, so precise control over current density and etching time were achieved, and then it is resulting in a good control of the refractive index and thickness over the individual layers forming the multilayer. The program is a LabView virtual instrument realized to control the fabrication process of monolayer and multilayer of porous silicon with a friendly interface. The program controls the different parameters of the electrochemical process via GPIB. Those parameters include two current steps (to form layers with different refractive indices), duration time of each step (to determine the thickness of each layer), delay time (time between two consecutive electrochemical currents), and number of period (number of multilayer structure).

Fig. 1. Electrochemical etching setup for fabricating PS layers

2.2 Silicon samples

The initial Si-crystalline wafers, n-type with resistivities of 1-5 Ω.cm and p-type with resistivities of 0.01-1 Ω.cm, were used for constant potential and constant current ECD, respectively. For the case of n-type silicon substrates we need to illuminate the back side of silicon wafers. Resistivity of silicon wafer strongly affects on quality of porous silicon layers. High resistivity wafer often makes porous silicon layers with rough surface and easily peeled off from Si-substrate during fabrication or drying process, while the low resistivity sample have more flat surface of porous silicon layers. In order to form Ohmic contacts on the samples, we deposited pure gold (Au) and/or aluminum (Al) on the back faces of the n- and the p-type samples, respectively. The Si-crystalline wafers were anodic etched in a HF-ethanol solution with HF concentrations from 10% to 30% at a constant current density of 10-60 $mA.cm^{-2}$ for time durations from some seconds to 15 minutes for controlling the refractive index of the PS layers. If the current density is modulated during the anodization, alternating layers of different porosities are formed as the silicon dissolution occurs primarily at the etched front PS/silicon substrates (Frohnhoff et al., 1995). Although the interface roughness between stacks is about 10-20nm, light scattering at these interfaces turned out to be very low. For this reason such layer stacks can act as optical waveguides and/or interference filters if the refractive indices are chosen properly (Krüger et al., 1998).

3. Active waveguide based on SRSO thin films

Initially, Canham proposed that the up-shift of the luminescence spectrum into the visible was due to quantum confinement in the silicon crystalline wire structure and that the hydride passivation of the Si wire was the reason for the high efficiency of the observed photoluminescence (PL). For a short time after that, spectroscopic studies conducted particularly on the polarization of the PL (Kovalev et al., 1996) and on features observed under conditions of resonant excitation (Calcott et al., 1993) have provided strong positive confirmation of the quantum confinement model. However, there were a lot of spectroscopic phenomena that can not be explained by the simple quantum confinement model. As such, numerous models have been put forward as alternative explanations for the PL from PS such as hydrogenated amorphous silicon, surface hydrides, defects, molecules, surface states (Amato & Rosenbauer, 1997). It is well known that in PS the surface to volume ratio is very large, so the surface effects are expected to have a significant influence on the material properties, especially optical ones (Kanemitsu et al., 1993). Because the Si atoms in Si nanocrystals are either at the surface or a few lattice sites away, the arrangement of interfacial atomic bonds, i.e. the passivation with Si-H or Si-O bonds, strongly affects the energy distribution of electronic states (Wolkin et al., 1999). In order to study PS as low-dimensional photonic materials, we elaborate on the effect of ageing on the spectral, intensity and lifetime of PL from the silicon nanocrystals in PS. Experimental results show that the effect of ageing on the spectral, intensity and PL lifetime of PS depends on the size of silicon nanocrystals. We focus our attention on strong emission properties and employ PS as a material for light emission sources, i.e. light emitting diodes and micro-cavity lasers operated in the visible region. In concentrating on the controllable changes in the refractive index of PS, we would like to use PS as a material for photonic devices such as planar optical waveguides, optical waveguide amplifier, optical interference filters, etc. As an optical material, we present the fabrication method for silicon rich silicon oxides (SRSO) thin films and properties of planar optical waveguides, active optical waveguides and optical interference filters operated in the range of infrared wavelengths. The advantage of optical waveguide amplifier based on Erbium doped SRSO is the efficient energy transfer from electron-hole pairs generated in the Si nanocrystals to their near erbium ions, which decay by emitting light at 1540nm. The excitation cross-section of Er-ions in Er-doped SRSO is increased more than two orders in comparison of this one in the Er-doped silica glasses (Friolo et al., 2001), so that the pump efficiency in Er-doped SRSO waveguides can be very high.

3.1 Porous silicon as a low-dimension photonic material

In the first part of this section we explain the effect of surface states on the PL properties of PS based on the ageing process in air. In the last part, we present the reason for the intense and stable luminescence of blue region which has been of great interest in recent studies (Gorelkinskii et al., 2008). Previous studies on the interaction of oxygen in air on the as-prepared PS (Wolkin et al., 1999) show that: I) the as-prepared samples were well passivated by hydrogen and free of oxygen, ii) after exposure to air the samples were gradually passivated by oxygen, and the red-shift of PL spectral occurred as samples exposure to air and was nearly completed after ageing of 24 h. It was suggests that the ageing process can be divided into two periods: the first one in which the transition of the luminescence mechanism occurs after exposing the sample to air for a short time, and the second one in which the non-radiative center concentration is changed by oxygen passivation (Bui Huy et al, 2003).

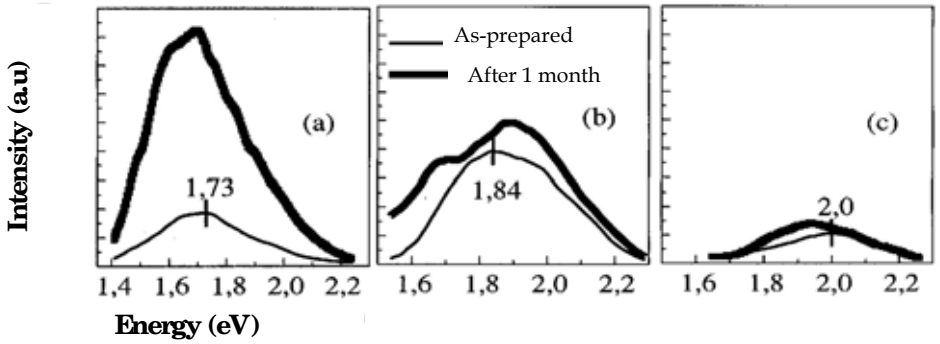

Fig. 2. PL spectra of the as-prepared samples and after exposure to air for 1-month; samples, denoted as 1,2 and 3, were prepared by the anodic etching in 20%, 13% and 10% HF solution, respectively. (a) sample 1, (b) sample 2 and (c) sample 3

In order to investigate the effect of surface passivation on the size of Si nanocrystals, a series of PS samples denoted as 1, 2 and 3 were prepared by anodic etching in 20%, 13% and 10% HF solution respectively. As seen in figure 2, the PL peaks of the as-prepared samples 1, 2 and 3 have energy levels of 1.73, 1.84 and 2.00 eV respectively. This is related to a decrease of particle size in the considered samples. The figure also reveals that the ageing produces a pronounced increase in PL intensity in sample 1 and only a slightly increase in samples 2 and 3. As seen in figure 3, the decay rate of the as-prepared samples (the curves 1a, 2a and 3a) shows that the concentration of non-radiative centers in sample 1 is higher than those in samples 2 and 3. The pronounced increase in intensity (in figure 2) as well as the pronounced decrease in decay rate (in figure 3) of sample 1 could be caused by the oxygen passivation of non-radiative defects. In samples 2 and 3 containing smaller particles, the initial passivation degree is higher, therefore the ageing is expected to induce a small change both in intensity and decay rate. The data comparison from curves 2a and 2c in figure 3 reveals that the modification of emission mechanism has no effect on the decay rate as well as its energy dependence $\tau^{-1}(E)$. This result seems to indicate that the replacement of Si-H bond by a Si-O one acting as a radiative center has no effect on the lifetime.

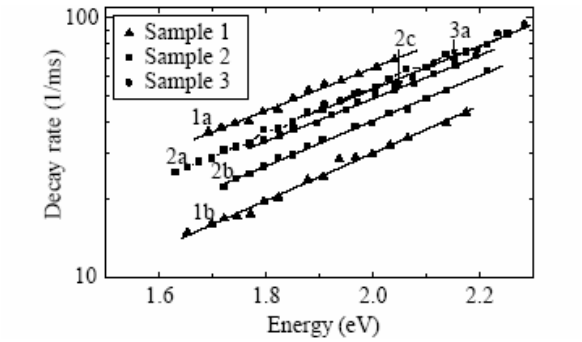

Fig. 3. Evolution of decay rate as a funtion of emission energy from sampes after preparation, curves 1a, 2a, 3a and after exposure to air for 1-month, curves 1b, 2b. Curve 2c coresponds to sample 2 for 24 h (Bui Huy et al., 2003).

Figure 2 and 3 established the relation between the size of particle, intensity and decay rate during ageing. In the sample containing larger nanocrystals, the change in intensity and decay rate, i.e. the luminescence lifetime, is much larger compared with that of the smaller nanocrystals during ageing process.

Figure 4 shows the evolution of PL spectra, measured at the end of an excited pulse after different exposure times. The figure reveals that the blue zone with the PL emission peaked at 470 nm is only observed after 72 hours of exposure to air. Furthermore, the figure also reveals that the PL intensity increases with increasing air exposure time. These observations differ from those reported by Volkin et al. (Wolkin et al., 1999) in which the intensity of blue emission from the as-prepared sample containing the small Si particles was shown to decrease as the exposure time increased. This result indicates that the blue-light emission observed in the present work does not originate from very small nanocrystals. Curve 4im shows the PL spectrum of a sample, which was exposed to air for 94 hours and then immersed in HF: ethanol solution. In comparing curves 4 and 4im, one can state that the blue zone in the PL spectrum observed for the sample after 94 hours of exposure to air is completely quenched. This quenching clearly relates to the fact that the silicon oxide layers in the exposed sample have been removed. The above results indicate that the intense and stable emission in the blue zone of the PL spectra observed in the considered samples relates to defects in silicon oxide layers.

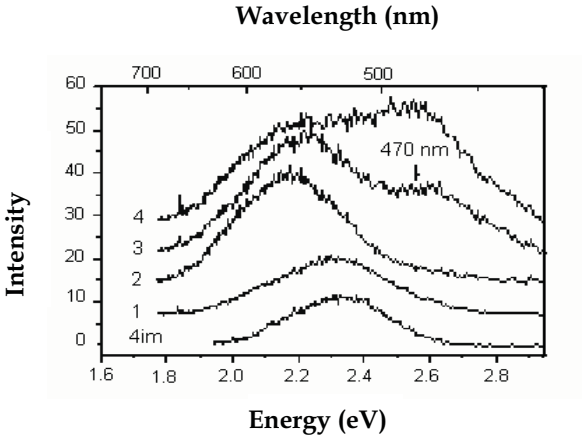

Fig. 4. Evolution of PL spectral measured at the end of excitation pulse from a PS sample after different exposure time (1): as-prepared, (2; 3; 4): after 26, 72 and 94 h of exposure to air, respectively, (4im): corresponding to sample exposed to air for 94 h. and then immersed in 5% HF: ethanol solution for 10 sec (Bui Huy et al., 2006).

3.2 Fabrication and characteristics of SRSO planar and active optical waveguides

In this section, before elaborating on the fabrication method and properties of planar optical waveguide, active optical waveguides, and optical interference filters based on SRSO thin films we explain the method of production for the PS multilayer which forms the basis for these devices.

The production of PS multilayer is possible because: (i) the etching process is self-limited (i.e. once porous layer is formed, the electrochemical etching of this layer stops); (ii) the

etching occurs mainly in correspondence between the pore tips; (iii) the porosity depends only upon the current density once the other etching parameters are kept fixed; and (iv) the refractive index of PS depends on its porosity (Mazzoleni & Pavesi, 1995). Therefore, by varying the current density during the etching process, it is possible to vary porosity in the etching direction. In this way, the formation of a stack of PS layers of different porosities (and hence, different refractive indices) results in a dielectric multilayer.

Our process for preparing an optical planar waveguide consists of 2 steps: making a PS film which contained a core layer and a cladding one, and stabilizing the waveguide structure by thermal annealing at high temperature in oxygen ambient for obtaining SRSO. In the process of fabricating an active optical waveguide, a step of deposition of Er ion into the PS film was carried out before thermal annealing. The high temperature treatment can cause an optical activation of Er ions in SRSO.

The PS films were formed by electrochemical etching of 1Ωcm p-type Si wafers in 30%HF: ethanol solution. The top core layer was fabricated by applying current density of 15mA/cm^2 for 7 min. The cladding was formed in the same way, with current density of 65mA/cm^2 for 3 min. These conditions allowed the core and cladding to have a porosity of about 60% and 65%, respectively. For Er-deposition on the PS layer, the PS layers were immersed in an Er-content solution, and a negative bias, relative to a platinum electrode, was applied to the PS samples for a certain time so that Er-ions were drawn into the pores of the PS. In the constant current ECD method, an $ErCl_3$–ethanol solution with an Er-concentration of 0.2 mol / liter was used, and the drift current was changed from 0.17mA.cm^{-2} to 0.45mA.cm^{-2} to obtain different Er-concentrations in the PS layers. To enable the optical activation of Er ions distributed in the pores of the PS layer, the sample was annealed at 400^{0}C for 2 h. For making the SRSO layers, we thermally annealed the samples at 800^0 - 950^{0}C in oxygen ambient for a short time (5-30 min.) and kept samples for a longer time in nitrogen gas at 1100^{0}C.

Figure 5 presents the FE-SEM image of a two-layer SRSO with different refractive indices ($n_{core} > n_{clad}$), which had been controlled by using current density of 20 and 30 mA.cm^{-2} for the core and the cladding layers, respectively. Based on the contrast between the core and the cladding due to the difference in porosities, it is observed that the film consisted of two layers in which the core layer thickness is about 4.5 μm, and the cladding about 7 μm. The thickness of layers depended on the time duration of electrochemical process, and layers of up to tens of microns could be grown.

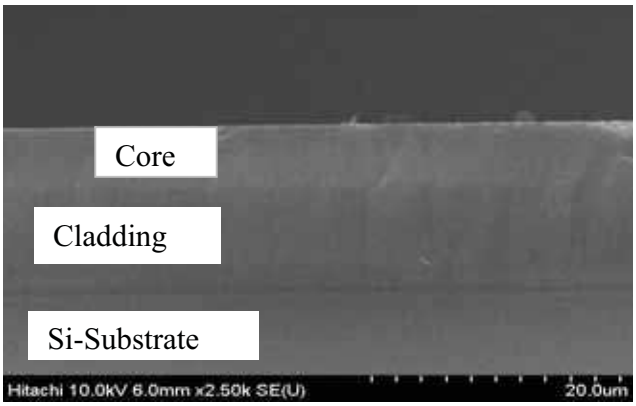

Fig. 5. FE-SEM image of bi-layer SRSO on a silicon substrate.

Figure 6 shows the HRSEM image of the surface of the core and cladding before (PS layer) and after (SRSO layer) of thermal annealing. As seen from Figures 6a and 6c, the difference in the density of the black area and the pores in the PS layer show that the porosity in the core layer is lower than that in the cladding. From this image we also observed the differences in density of the black area and the contrast between the black area and the white one from the PS layers (Figures 6a and 6c) and SRSO layers (Figures 6b and 6d). Those differences suggest that the treatment can cause a decrease in the size of pores and the porosity of SRSO layers. The prepared SRSO layers were dense and therefore the optical properties of the waveguides were stabilized.

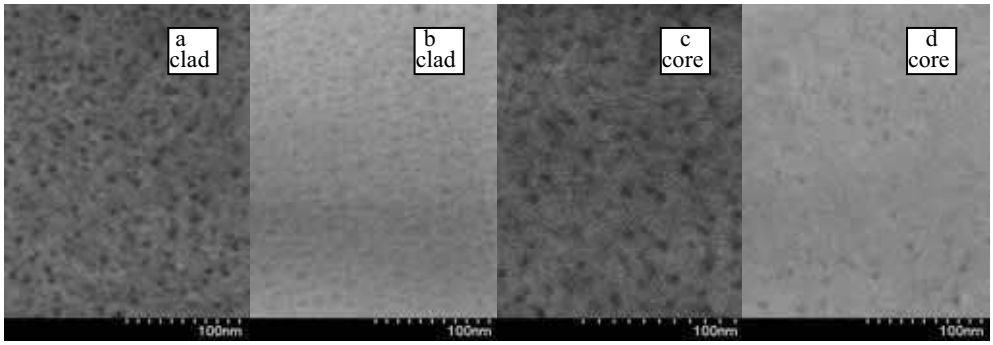

Fig. 6. FE-SEM image of surface of the core and cladding of PS layer (a, c), and of SRSO layer (b, d), which was obtained before (a, c) and after (b, d) thermal annealing in order to estimate their porosities.

Samples	Sample layers	Refractive index	Thickness (μm)
Series No.1	Core layer	1.4512	5.54
	Cladding layer	1.4275	3.35
Series No.2	Core layer	1.6088	1.908
	Cladding layer	1.5402	6.239

Table 1. Parameters of SRSO waveguide samples

The waveguide properties of the SRSO multi-layers were characterized by using M-line spectroscopy with the Prism-coupler method (Metricon 2010/M), which has the capacity to measure the thickness, the refractive index and the wave-guided modes in thin films with high accuracy (±0.0005 for index). The number of wave-guided modes in the SRSO waveguide strongly depended on the thickness of the core layer. Figure 7(a) shows that a single mode of 1310 nm in wavelength could be guided in a core layer with a thickness of 1.9 micron. The measured indices of this sample were 1.6088 and 1.5402 for the core and the cladding layers, respectively. Figure 7(b) demonstrated the measured indices and the two-mode waveguide at a 1310-nm wavelength for a core layer with a thickness of 5.54 microns. The measured indices were 1.4522 and 1.4275 for the core and the cladding, respectively. This result shows that, by changing the current density in the ECD process, we can obtain a planar layer with different indices that support the waveguide properties in the layer. The Er-ion distribution in the SRSO layer was characterized by using the EDX method with the SEM technique. The Er-ion concentration, which was doped into PS, could be controlled by using an Er-content solution

and by using the current density in the ECD method. For the purpose of obtaining high-concentration Er-doped SRO materials (more than 0.1 atomic % of Er) without Er clusters, which would be good candidates for planar-waveguide amplifiers, we carried out a very careful study of the distribution of Er ions along the depth of the SRSO layer.

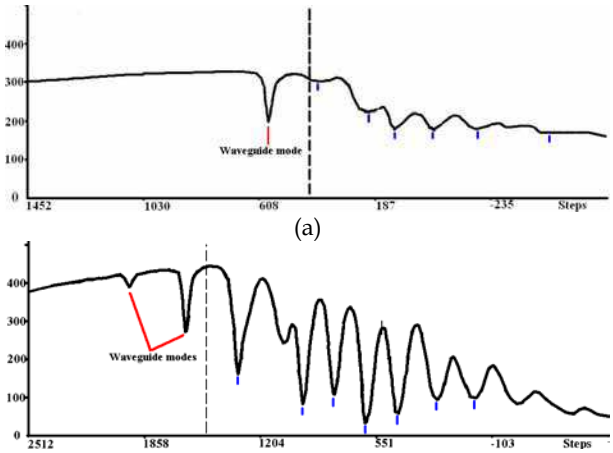

Fig. 7. Waveguide properties of the SRSO core/cladding layers. (a) Single-mode in the sample with core/cladding thickness of 1.90/6.24 μm and indices of 1.6088/1.5402 (b) Multi-mode in the sample with core/cladding thickness of 5.54/3.35 μm and indices of 1.4512/1.4275.

Samples	Type and resistivity	HF concentration (%)	Er-drift current ($mA.cm^{-2}$)	Annealing (^0C)
BH-10	p-type, 1 Ωcm	30	0.17	950
BH-11	p-type, 1 Ωcm	25	0.20	950
BH-12	p-type, 1 Ωcm	20	0.17	950
BH-13	p-type, 1 Ωcm	30	0.20	820
BH-14	p-type, 1 Ωcm	25	0.25	950
BH-15	p-type, 10 Ωcm	30	0.17	950
BH-16	p-type, 1 Ωcm	25	0.45	950

Table 2. Preparation conditions of Er-electrochemically-doped SRSO samples

Figure 8a shows a SEM image of the Er-doped SRSO wave-guide layer prepared by using the ECD method with a drift current density of $0.2mA.cm^{-2}$. The measurement was carried out for an Er-doped SRSO thickness of 5 microns, and the Er-ion concentration was measured at points along the depth of the SRSO layer. The Er-ion concentration increased from 0.11 atom % at the top surface to 0.2 atom% at the depth of 3.5 micron from the top surface. The Er-ion concentration decreased with further increased in the depth inside the samples (see fig. 8b). For the characterization of optical properties of Er-doped SRSO layers, the Nitrogen gas laser (LN 1000, λ=337.1nm) an Argon laser (Coherent Inova 300, λ= 488nm) and a 1-W continuous laser diode (λ=976nm) were used as optical excitation sources. The

luminescent emission from the samples was collected by using two optical fibers located at 10 mm from the sample surface. The luminescence emission was analyzed by using a Jobin-Yvon spectrometer (HR460) with a multi-channel Charge-Coupled Device (CCD) detector and by Triax 320 spectrometer with a C7211 Hamamatsu CCD infrared detector for visible and infrared light, respectively.

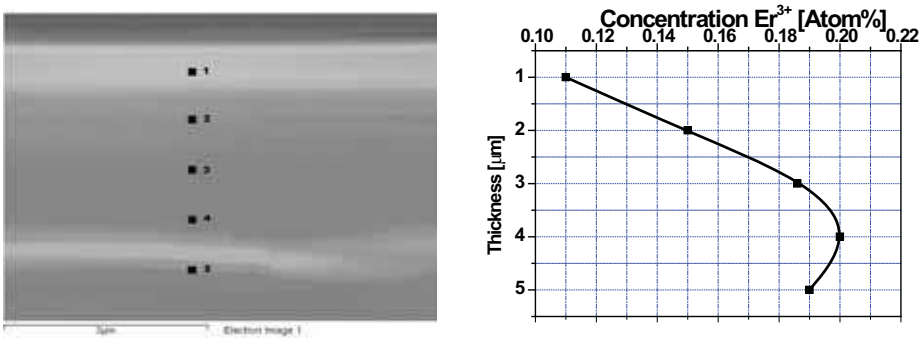

(a) (b)

Fig. 8. FE-SEM image of Er-doped SRSO layers on a Si- substrate with the Er-concentration measured at points along the depth of the layer by using EDX method (a) and the Er-ion distribution inside the sample (b).

The first criteria for the Er-doped SRSO samples were that they could be in both optically activated centers: the Si-nanocrystal induced visible light and the Er ion induced infrared light. Our experiment shows that the samples without thermal annealing did not emit IR light, but after thermal annealing, they strongly emitted in the 1540-nm range. This fact shows that thermal annealing at high temperatures for obtaining Er-doped SRSO layers is an important condition for optical activation of Er ions.

In general, the intensity of luminescence emission at 1540 nm will be increase with increasing concentration of Er ions in the SRSO layer (Elhouichet & Oueslati, 2007), when the Er-ion concentration reaches its saturation value, the luminescence intensity at 1540 nm will be decreased due to the quenching effect from Er-ion clusters (Kit & Polman, 2000). Figure 9 presents the luminescence spectra at 1540 nm for samples with different drift currents from 0.17 to 0.45mA.cm^{-2} under excitation by 976-nm laser beam. The 1540-nm luminescence intensity of all the samples increased with increasing drift current density from 0.17 to 0.25mA.cm^{-2}, but when the drift current density was more than 0.25mA.cm^{-2} the luminescence decreased slightly with increasing drift current.

The evidence of energy transfer can be obtained by changing the wavelength of the excitation source. The pump at 976 nm only caused a direct excitement of Er ions (from $^4I_{15/2}$ to $^4I_{11/2}$ level), whereas the pump at 488 nm caused both a direct excitement of Er ions (from $^4I_{15/2}$ to $^4F_{7/2}$ level) and an indirect one related to the energy transfers from Si-nc to Er ions. As the effective Er excitation cross-section in the Er-doped SRSO layer is more than two orders of magnitude higher with respect to the Er resonant absorption of a photon, the pump at 976 nm causes a linear dependence of intensity on excited power (Najar et al., 2006) and the pump at 488 nm causes the non-linear one as seen in Figure 10. The photoluminescence intensity of samples irradiated by a 976-nm wavelength increased linearly with increasing excitation power when the PL emission of the sample pumped at a 488-nm wavelength has reached saturation at high power.

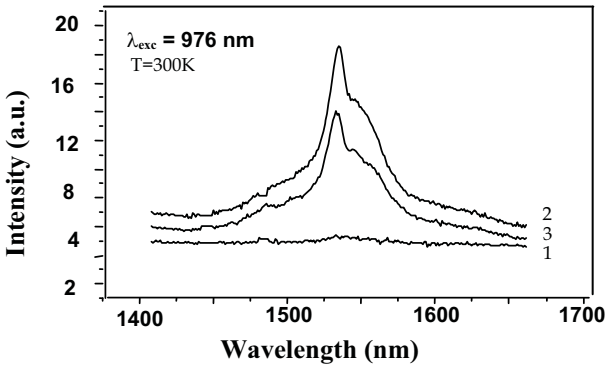

Fig. 9. Luminescence spectra from samples 1, 2 and 3 under drift current density of 0.17, 0.25, and 0.45mA cm^{-2}, respectively.

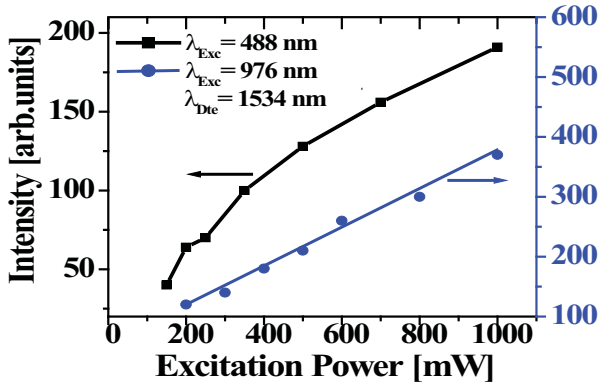

Fig. 10. Dependence of luminescence intensity of Er-ions at 1534 nm on the power of the excitation laser at wavelengths of 488 nm and 976 nm.

4. Interference filters based on porous silicon and silicon-rich silicon oxide layers

Interference filters based on PS were realized for the first time in the last decade (Vincent, 2004). They are formed from silicon wafers by electrochemical etching in HF solution. Compared with other methods, the electrochemical etching method avoids the difficulty associated with the stacking and assembly of dielectric layers, eliminates the need for the lengthy deposition of thick films, and permits a wide range of refractive indices to be fabricated from a single silicon substrate. PS interference filters usually formed from different dept profiles of the refractive index of PS multi-layers which act as Bragg reflectors. The optical thickness of the high- (n_H) and low-refractive index (n_L) layers are 1/4 of the filter wavelength, so that these structures are usually called quarter-wave-stacks (Kruger et al., 1998). The effective refractive index of PS layer is mainly determined by the porosity which can be varied by several anodization parameters. The most suitable way is changing

the anodization current density, with high current densities resulting in high porosity and low refractive index. However, one of the main problems concerning the use of PS interference filters is the ageing of the PS: due to the large inner surface of the porous silicon the material oxidizes very fast compared to bulk silicon. This phenomenon is well-known from emitting PS layers, which was discussed in the section 3 of this chapter. For PS interference filters the natural oxidation is disturbing as well as it causes a change of the refractive index and of the PS layer thickness (Barla et al., 1986), which results in the following ageing effects: (i) a blue-shift of the filter wavelength; (ii) a decrease of the filter performance, if the change of the optical thickness is different for the n_H and n_L layers; (iii) a continuous decrease of reflectivity, which depends on the refractive index ratio n_H / n_L. The ageing effect of the PS quarter-wave-stacks could be strongly reduces by a thermal annealing process to obtain SRSO structure.

4.1 Simulation of the PS interference filters

4.1.1 Mathematical model

Before fabricating the interference filters based on multi-layer structure, a simulation program was set up in order to design and predict the optical properties of interference filter based on quarter-wave-stacks. Each quarter-wave stack system is characterized by the following basic parameters: number of layers, refractive indices, and optical thicknesses of layers. The computation of reflectivity and transmission spectrum from the above parameters has an important role in knowing thoroughly about multilayer system. There are many numerical methods for analyzing the multilayer system such as Transfer Matrix Method, Plane Wave Method, and Finite Difference Time Domain. In our work we use Transfer Matrix Method (TMM) for simulation of reflectivity and transmission of interference filters. The TMM can handle any number of layers in a multilayer structure. In addition, these layers can be ordered in any manner and there is no requirement that they should be periodic. Even if they are periodic, the unit cell that is repeated does not have to be composed of two layers only, but any number of layers. There is also no restriction on the thickness of any layer. The thickness and the refractive index of each layer can be defined independently. This makes the TMM most suitable for modeling structures formed by different periodic multi-layers stacked together, since they are not fully periodic. The TMM can also handle structures having a high index contrast between their two composite materials contrast material systems. This makes the TMM suitable for modeling multilayer structures, which usually have a high index contrast between their composite materials.

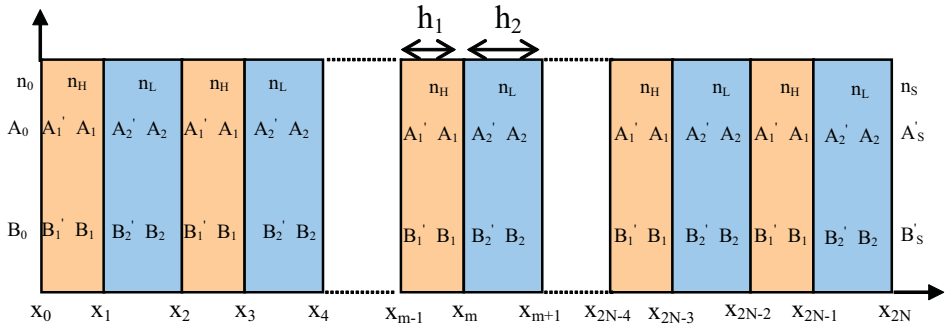

Fig. 11. Diagram of multi-layer interference filters.

We consider quarter-wave-stacks as a structure containing of N bi-layers of porous silicon with periodic refractive indices that are coupled with a medium with refractive index n_0 at the interface and a substrate with refractive index n_s at the bottom. As can be seen form Fig.11, the configuration of interference filter is a periodic structure of two porous silicon layers ($n_H \mid n_L$). $A(x)$ represents the amplitude of the right-traveling-wave and $B(x)$ is that of the left-traveling one and $A(x)$ and $B(x)$ are not continuous at the interfaces. The thickness of each layer is h_m, n_m is the refractive index and $\Lambda = h_m + h_{m+1}$ is a period of structure.
The dielectric structure is defined by (Saleh & Teich, 1997):

$$n(x) = \begin{cases} n_0, x < x_0 \\ n_H, x_0 < x < x_1 \\ n_L, x_1 < x < x_2 \\ \dots \\ n_s, x_{2N} < x \end{cases} \tag{2}$$

Where n_0, n_s are refractive indices of the incident medium (ambient) and of the substrate, respectively. With this structure, we have $n(x) = n(x+\Lambda)$. In general, for the m-th layer, the refractive index is n_m and thickness is d_m in which $d_m = x_{m+1} - x_m$ $(m=1:2N)$.
The electric field of a general plane-wave can be written as $E=E(x)\, e^{\,i(\omega t - \beta z)}$ where $E(x)$ is the electric field distribution and can write as:

$$E(x) = \begin{cases} A_0 e^{-ik_{0x}(x-x_0)} + B_0 e^{ik_{0x}(x-x_0)}, x < x_0 \\ A_m e^{-ik_{mx}(x-x_m)} + B_m e^{ik_{mx}(x-x_m)}, x_{m-1} < x < x_m \\ A_s' e^{-ik_{sx}(x-x_{2N})} + B_s' e^{ik_{sx}(x-x_{2N})}, x_{2N} < x \end{cases} \tag{3}$$

Where k_{mx} is the x-component of the wave vector, $k_{mx} = \omega n_m \cos\theta_m / c$ and θ_m is the ray angle in each layer. A_m and B_m are the amplitude of plane waves at interface $x=x_m$.
If we write the two amplitudes of $E(x)$ as a column vector, the plane waves at different layers can be related by:

$$\begin{pmatrix} A_{m-1} \\ B_{m-1} \end{pmatrix} = D_{m-1}^{-1} Dm \begin{pmatrix} A_m' \\ B_m' \end{pmatrix} = D_{m-1}^{-1} D_m P_m \begin{pmatrix} A_m \\ B_m \end{pmatrix}, \quad m=1, 2 \dots 2N \tag{4}$$

Where the dynamical matrices D_m are written by:

$$D_m = \begin{cases} \begin{pmatrix} 1 & 1 \\ n_m \cos\theta_m & -n_m \cos\theta_m \end{pmatrix} & for\, TE\, wave \\ \begin{pmatrix} \cos\theta_m & \cos\theta_m \\ n_m & -n_m \end{pmatrix} & for\, TM\, wave \end{cases} \tag{5}$$

And the propagation matrix P_m can be written by:

$$P_m = \begin{pmatrix} e^{ik_{mx}h_m} & 0 \\ 0 & e^{-ik_{mx}h_m} \end{pmatrix} \tag{6}$$

Thus the relation between A_0, B_0 and $A_S^{'}$ and $B_S^{'}$ can be written as:

$$\begin{pmatrix} A_0 \\ B_0 \end{pmatrix} = D_0^{-1}\left[D_1 P_1 D_1^{-1} D_2 P_2 D_2^{-1} \ldots \right]^N D_S = \begin{pmatrix} M_{11} & M_{12} \\ M_{21} & M_{22} \end{pmatrix} \begin{pmatrix} A_S^{'} \\ B_S^{'} \end{pmatrix} \tag{7}$$

From the matrix elements, we can calculate the reflectance and transmittance of monochromatic plane waves through a multilayer structure. If the light is incident from medium n_0, the reflection and transmission coefficients can be calculated as:

$$\begin{aligned} r &= \left(\frac{B_0}{A_0} \right)_{B_S=0} \\ t &= \left(\frac{A_S}{A_0} \right)_{B_S=0} \end{aligned} \tag{8}$$

Using the matrix equation (7), we have:

$$\begin{aligned} r &= \left(\frac{M_{21}}{M_{11}} \right) \\ t &= \left(\frac{1}{M_{11}} \right) \end{aligned} \tag{9}$$

Then the reflectance is:

$$R = \left| \frac{M_{21}}{M_{11}} \right|^2 \tag{10}$$

Where ambient with refractive index n_0 is lossless.

4.1.2 Simulation program

From the above-mention theory, we can set up a program for the simulation of multilayer structure by using Matlab. This program contains the following parameters:

- Refractive index of ambient is n_0: the medium from which the incident wave arrives to the surface of the first layer of multilayer structure.
- Refractive index of substrate is n_s: Substrate can be the silicon wafer or other medium.
- Incident angle (θ): The angle between the propagation direction of the incident wave and the normal to the surface of layers. This layer can vary from 0 to 90 degrees.
- Number of bi-layer (N): number of periodic multilayer of interference filter.
- Refractive indices (n_m) and thickness (h_m) of layers. They can be either n_H, d_1 or n_L, d_2.
- Wavelength range: the range from the initial to the final values of wavelength for analyzing reflectivity spectra.

4.1.3 Results of simulation

The refractive index ratio n_H/n_L of the interference filter strongly influences on the width and the sharpness of the filter wavelength band. Figure 12 shows the calculated reflection spectra of three filters with 12 periods and the thickness of one layer was calculated to obtain a centered reflection wavelength at 1550 nm. The calculated values of refractive

indices in the range of 1.5 to 2.5 are often obtained from prepared porous silicon layers. We surmised that the line-width and sharpness of the spectra are influenced by the ratio of n_1/n_2 and the increase of n_1/n_2 leads to the spectral broadening.

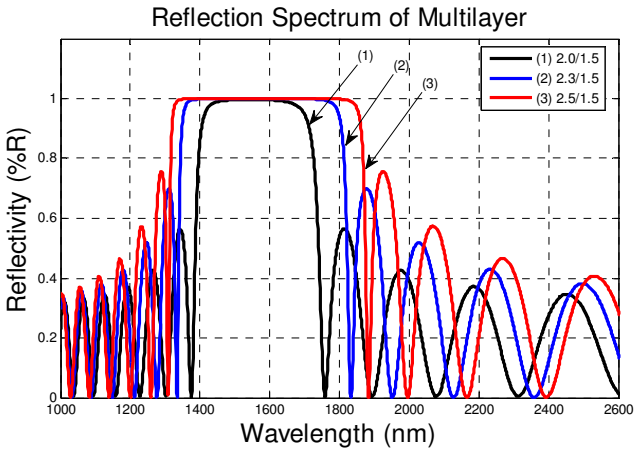

Fig. 12. Reflection spectra of multilayer structures with different ratio of n_H/ n_L

The influence of the number of periods (N) of multilayer structure on the reflection spectra demonstrates in Figure 13. When N increases, the reflection spectra are sharper, narrower and the reflectivity tends to unity. The simulation results can be used for design interference filters based on both of PS and SRSO materials.

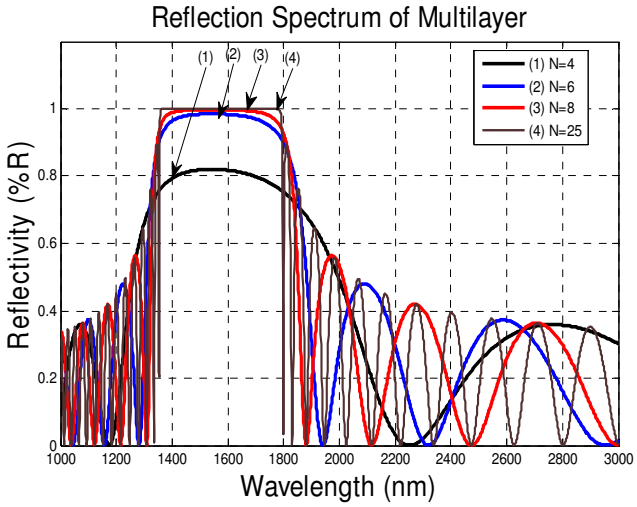

Fig. 13. Dependence of reflectivity upon period number of periods of multilayer structures with ratio n_H/n_L of 2.5/1.5, corresponding to period numbers 4, 6, 8 and 25, respectively.

4.2 Fabrication of interference filters based on PS and SRSO multilayer

The porous silicon multilayer was fabricated using electrochemical etching of highly doped p-type (100) silicon wafers with resistivity of 0.01- 0.1Ω.cm in 13%-20% hydrofluoric acid (HF): ethanol solution. The electrochemical process was carried out without illumination. The process was monitored by computer-controlled current source Autolab PGS-30, so precise control over current density and etching time was maintained, thus resulting in good control over the refractive index and thickness of the individual layers forming the multilayer. The multilayer was formed by periodically varying the applied current density between two levels (J_1 and J_2) of 64 and 19 mA/cm^2 respectively, as presented in Figure 14. The number of periods for each filter was from 6 to 18. The silicon pores and multilayer structures of the filter were analyzed by Field-Emission Scanning Electron Microscopy (FE-SEM). Figure 15 shows a FE-SEM-image of the completed porous silicon 12-period compose fabricated by ratio of current densities J_1/J_2 = 64/19 and duration time of 6.33 and 12.3 seconds, respectively. As seen in Figure 15a, the typical sizes of the silicon residuals and air voids are about 50 nm. This allows us to describe the PS layers as "an effective medium", whereby its optical properties mainly depend on its porosity. The SEM-image of the multilayer displays different gray levels depending on the porosity of the layers (see Figure 15b). Because of this, the layers of the stack are distinguished and therefore the thickness of each layer can be experimentally determined.

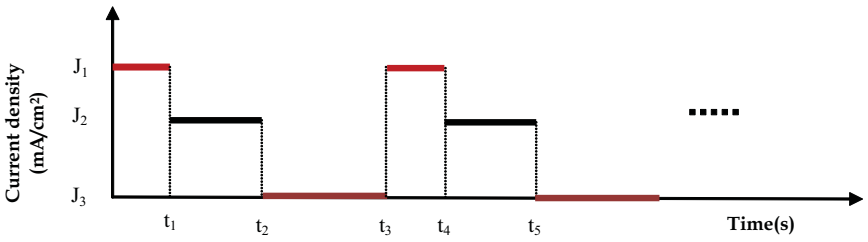

Fig. 14. Schematic of current density modulation versus anodization time

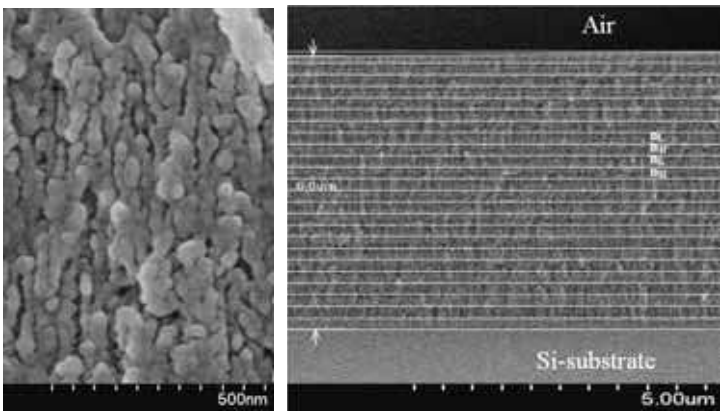

(a) (b)

Fig. 15. Cross-sectional SEM images of silicon pores (a) and multilayer structure of the interference filter with period number N=12 (b).

Figure 16 displays the reflection spectra of multilayer filters with different thickness levels. The curves (a), (b), (c) and (d) displays the reflection spectra of 12-period filters with a total thickness of 8.1μm, 6.0μm, 5.4μm and 4.5μm, respectively. The difference in the thickness of interference filters and therefore, the thickness of the layer in the stacks causes the shift of the center wavelength at which the reflectance would be maximal.

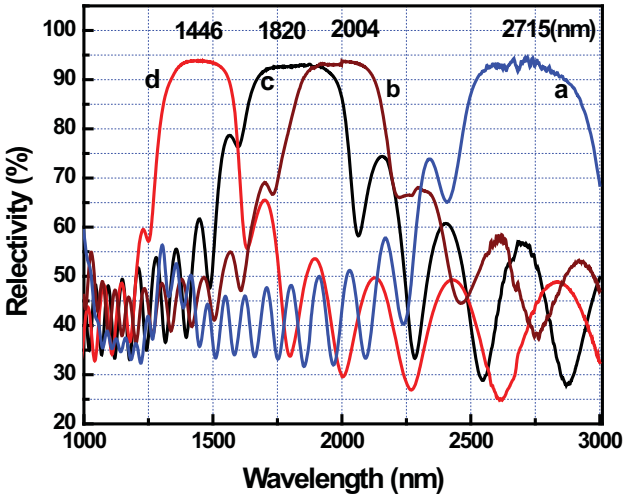

Fig. 16. Shifting the reflection spectra of 12-period filter by varying the thickness of the layers in the stacks: (a) h=8.1μm; (b) h=6.0μm; (c) h=5.4μm; (d) h=4.5μm.

Figure 17 shows the reflection spectra from two filters, denoted as M5 and M4, fabricated at a ratio of current densities J_1/J_2 = 64/19 and 38/19, respectively. The refractive index of PS layer depends on anodization current density, so that the refractive index contract between neighboring PS layers also depends on the ratio of current densities which created those layers. The increase in the FWHM (full-width at half-maximum) of the reflective spectrum from M5 filter compared with that from M4 one is due to the difference in the ratio of current densities (J1/J2) forming those filters.

Figure 18 shows the reflection spectra at wavelength of 1550 nm-range from three filters with a different numbers of periods. As seen from this figure, when period number increases the spectra become shaper, narrower and the refractivity increased. This result relatively corresponds to our simulation as shown in Figure 12.

The difference in the characteristics of filter spectra from the simulation and experiment occurs in the filters having too few or too many periods (N). In the case of filters having too few periods (N≤6), reflection from the interfaces, especially from the interface between air and the top layer, becomes more important in those filters, so that the imperfections of interfaces created by electrochemical etching can cause a deformation of the reflective spectrum as seen in curve (a) of Figure 18. In the case of the filters having too many periods (N≥18), the long anodization time causes a deformation of the nano-structure of surface layers whereas the nano- and micro-structure of the bottom layers can be affected by the slower transport of etching substances. All of these factors lead to a break in condition of the Bragg reflection in such layers and the decrease in reflectivity of the filter as shown in curve (b) of Figure 18.

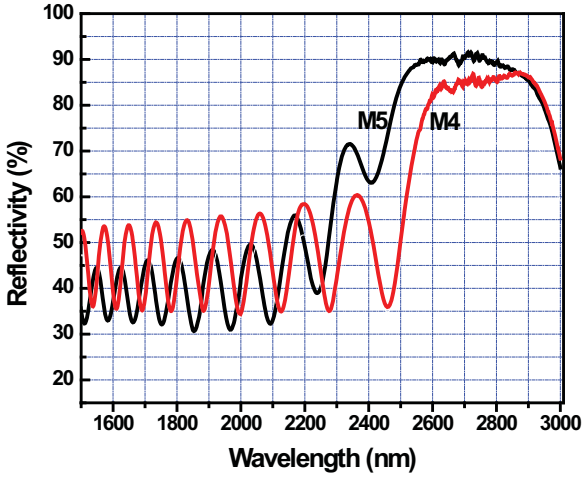

Fig. 17. Reflection spectra versus the refractive index ratio between nearest layers of PS interference filters.

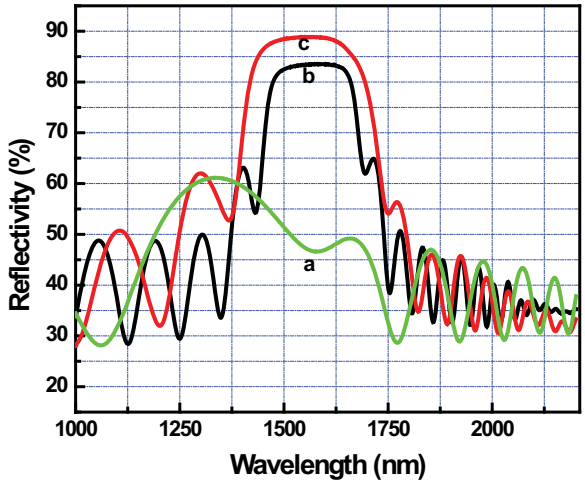

Fig. 18. Reflection spectra versus period numbers of stacks: curves a, b and c from multilayer filters with periods of 6, 18 and 12, respectively.

The interference filters have a big potential of applications not only for fiberoptic communication, but for bio-chemical sensory. The Table 3 shows an electrochemical etching process for making quarter-wave-stack filters operated at visible region, which is suitable for bio-chemical sensors. For making visible-range interference filters, we need decrease an etching time from tens seconds for IR region to some seconds for visible, while the current density is kept constantly.

Samples	Period numbers	Current density	Time (seconds)
Series No.1	12	J_1 = 50 mA.cm^{-2}	2.857
		J_2 = 15 mA.cm^{-2}	5.555
		J_3 = 0	8.0
Series No.2	12	J_1 = 50 mA.cm^{-2}	3.625
		J_2 = 15 mA.cm^{-2}	6.349
		J_3 = 0	8.0
Series No.3	12	J_1 = 50 mA.cm^{-2}	2.653
		J_2 = 15 mA.cm^{-2}	5.159
		J_3 = 0	9.5

Table 3. Electrochemical etching process for making interference filters at visible region

Figure 19 shows the reflection spectra of interference filters with reflection wavelength at 650nm-region, which prepared by etching process presented in table 1. When the etching time of electrochemical process increased, the reflection centered wavelength shifted to red-zone, i.e. the thickness of bi-layer stacks increased.

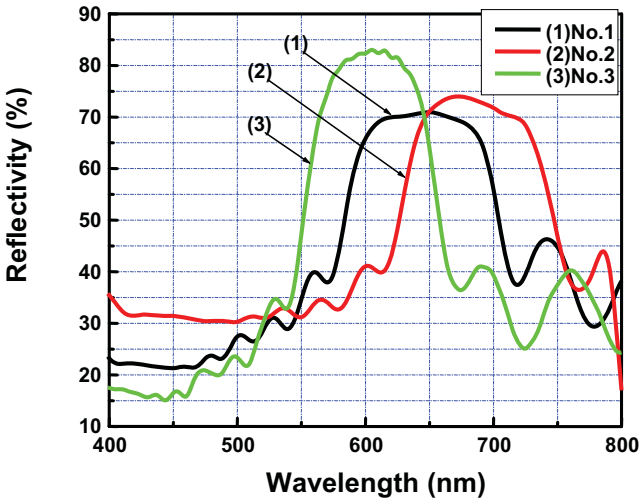

Fig. 19. Reflection spectra of red-light PS filters made by modulation of current density with different etching time.

We used thermal annealing process of samples for a stabilization of the optical properties of PS interference filters. The thermal annealing process of PS samples has three steps: i) first the PS samples were kept at 60^{0}C for 60 min in air ambient to stabilize the PS structures; ii) the pre-oxidation of PS samples was performed at 300^{0}C for different times varying from 20 to 60 min in oxygen ambient and iii) keeping the samples in Nitrogen ambient at the same temperature for 30 min and then the temperature decreased with very slow rate to room temperature.

Figure 20 shows the filter wavelength shift of as-prepared (PS) and pre-oxidized samples using the oxidation parameters 300^{0}C/40min, respectively. The thermal annealing process caused a blue-shift of reflection wavelength of 42 nm and slightly increases a reflectance of

the filters (about 6%) in our case. At high temperature of annealing process (for example: at 900^{0}C) filter wavelength still shifted to the shorter-wavelength zone the reflectance of filters would be strongly decreased. This can be explained as follows: the filter wavelength depends on the thickness of the bi-layer stacks which slightly decreased in the thermal annealing in oxygen ambient, while the reflectivity is determined by the refractive index ratio of the layers that may be decreased during oxidation process at high temperature.

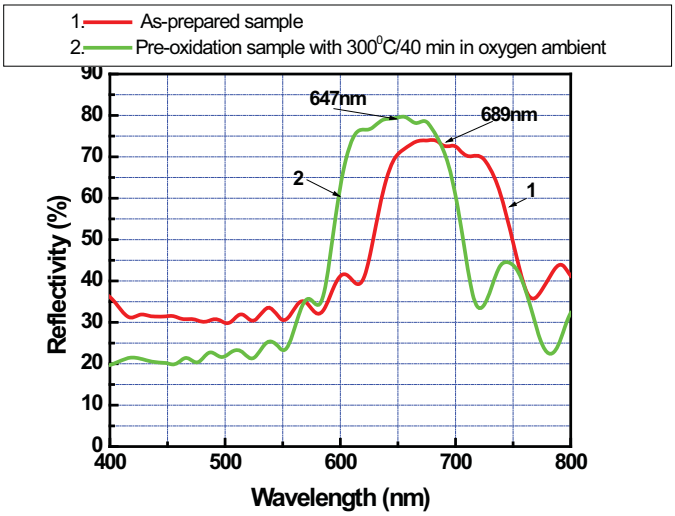

Fig. 20. Filter wavelength of as-prepared (1) and pre-oxidation (2) PS samples at 300^{0}C in oxygen ambient. The blue-shift of filter wavelength of 42 nm was obtained.

5. Micro-cavity based on porous silicon and silicon-rich-silicon oxide multilayer

The structure of micro-cavities, also called Fabry-Perot filters, consists of two parallel Distributed Bragg Reflector (DBR) separated by a spacer layer, whose reflective index can be the same or different to the ones used for the DBRs. The optical thickness of the spacer layer can be λ or $\lambda/2$ (Loni et al., 1996). The reflectivity spectrum of this structured material is characterized by a very narrow pass-band centered in a high reflectivity wavelength range. Micro-cavities can be used as band-pass filters with a tuned position of the peak (Weiss & Fauchet, 2003), tunable mirrors (Gao et al., 2002) and highly sensible detectors of substances like ethanol, methanol, acetone, chlorobenzene and nitrogen dioxide, among others (De Stefano et al., 2003; Volk et al., 2004; Anderson et al., 2003). They also have been used for optical sensor, biosensor and chemical sensor fabrication. In this section, we present the results of fabrication and investigate the wavelength-selective characteristics of DBR micro-cavity based on porous silicon multilayer structures. A simulation program for DBR micro-cavity based on the TMM has been developed from simulation program realized for interference filters that was shown in the subsection 4.1. Figure 21 shows the cross-sectional scheme of DBR micro-cavity with spacer of ds between two interference filters consisting N periods for simulation.

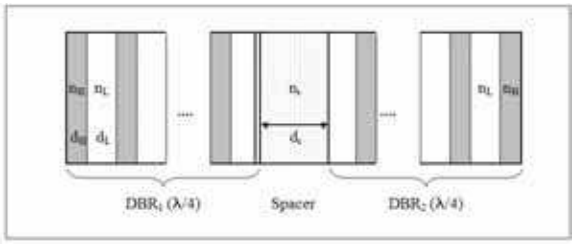

Fig. 21. Schematic of cross-section of DBR micro-cavity. The spacer layer with refractive index ns and thickness d_s should be inserted between two symmetric DBRs.

5.1 Simulation results for DBR micro-cavity

Figure 22 shows the simulated reflectivity spectrum of DFB micro-cavity for selective wavelength of 650 nm, which consists the spacer layer thickness of λ/2 and n_s=1.5 between two multilayer stacks of 4 periods with n_H=2.3 and n_L=1.5 for high and low refractive indices of layers, respectively. These parameters result in wide reflectance with a high reflectivity (100%) and sharp transmission band in the spectra of Fabry-Perot filters.

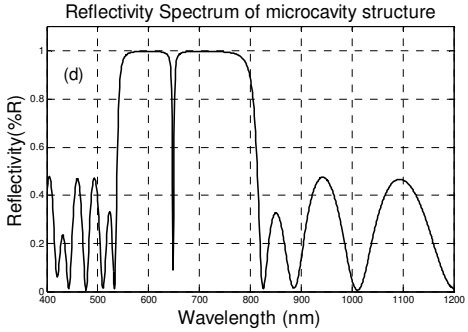

Fig. 22. Reflection spectrum of DBR micro-cavity with spacer thickness of λ/2 and refractive index of 2.5 inserted in between two 4-period interference filters. The selective wavelength of cavity designed at 650 nm.

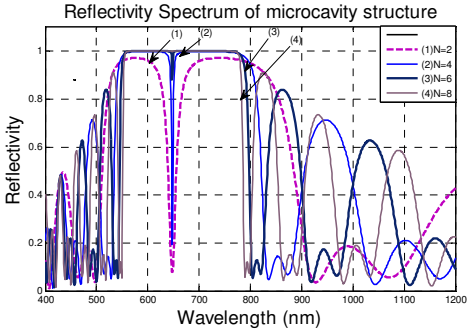

Fig. 23. Reflection spectra of a DBR micro-cavity at wavelength of 650 nm obtained by changing numbers of periods of DBR from 2 to 8.

The line-width of the transmission peak depends on the number of periods N of the DBR. When N increases, the transmission peak becomes narrower; the reflectivity of the band-gap increases and its edges became sharper. Simulation results show that the DBR micro-cavity has the band-pass width of 2 nm, the transmission of 90% at wavelength of 650 nm when the number of periods is more than 6 (see Figure 23).

5.2 Fabrication of PS and SRSO micro-cavity

Fabry-Perot PS micro-cavity has been formed by electrochemical etching of high doped *p*-type silicon wafers (resistivity of 0.01 ÷ 0.1Ω.cm) in an aqueous HF: ethanol electrolyte. The *p*-type silicon substrates yield the most favorable porous silicon morphology. The pores are large enough to allow infiltration of other species but interconnected and small enough to allow porous silicon to be treated as an optical medium for visible and infrared light. The electrolyte with concentration 16% HF and ethanol of ratio 1:2, respectively, is chosen because of the large porosity variation obtained by varying the etching current.

Description	Current density (mA/cm²)	Etching time (sec)
DBR on top (4.5 periods)	J_1=15	4.762
	J_2=50	2.857
Spacer layer (1 period)	J_3=(10-50)	5.714
DBR on bottom (5 periods)	J_1=15	4.762
	J_2=50	2.857

Table 4. Electrochemical etching conditions for making PS micro-cavities

Micro-cavity was formed by periodically varying the applied current density with two levels (J1 and J2) between 15 and 50mA/cm² and one spacer layer (J3). PS micro-cavities are formed by first etching a top DBR with alternating $\lambda/4$-thickness layers of low and high porosities (high and low refractive indices, respectively), then etching a $\lambda/2$-thickness spacer layer with the designed refractive index, and finally etching a bottom DBR with the same conditions as the top DBR. Detailed electrochemical etching conditions are presented in Table 4. The PS micro-cavities used in our cases typically consist of 4.5/5 period upper/lower DBR. Each period has a pair of low and high porosity layers. The PS micro-cavity samples have been rinsed in methanol and isopropanol after anodization process and dried in nitrogen atmosphere.

The micro- and nano-structures of the prepared PS micro-cavity have been analyzed by using the Scanning Electron Microscopy (FE-SEM Hitachi S-4800). Figure 24 shows the SEM cross-section of a PS micro-cavity made by electrochemical etching condition shown in table 4. It can be observed in Figure 24a that the SEM image shows the dark and bright layers that have a low and high porosity, respectively. Based on this difference, the layers of the stack are distinguished and therefore the thickness of each layer can be determined of about 165 nm. As seen in Figure 24b, the typical sizes of the silicon residuals and air voices are less than 30 nm. The measured reflection spectrum of PS micro-cavity is shown in Figure 25. The spectrum is characterized by a transmission band at 643.3 nm in between two high reflection bands. The reflective distinction ratio of 40% and the Full-Width-Half-Maximum (FWHM) band-pass width of 20 nm were observed in PS micro-cavity based on symmetrical 5-period DBRs.

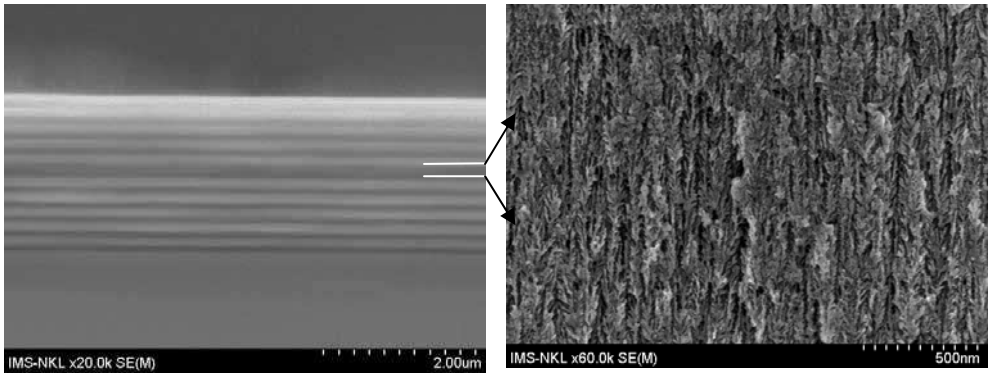

(a) (b)

Fig. 24. SEM cross-section of PS micro-cavity with λ/2-wavelength thickness spacer for centered wavelength of 650 nm (a) and PS size in the spacer layer (b).

The preparation of PS structures composed by several layers for DBR micro–cavity with narrow band-pass width of 2 nm as a design by simulation is difficult in practice, because the line-width of transmission of micro-cavity was strongly affected by homogeneity of the layers. The anodization condition might drift as the sample thickness and refractive index of stacks, and the solution composition changes with the depth because of limited exchange through the pores, that caused the different of experimental results in comparison with simulation one. In general, the band-pass width of 20 nm at the visible region obtained from the PS micro-cavity based on electrochemical etching technique is good enable for applications in the optical sensor, biosensors and/or micro-cavity lasers.

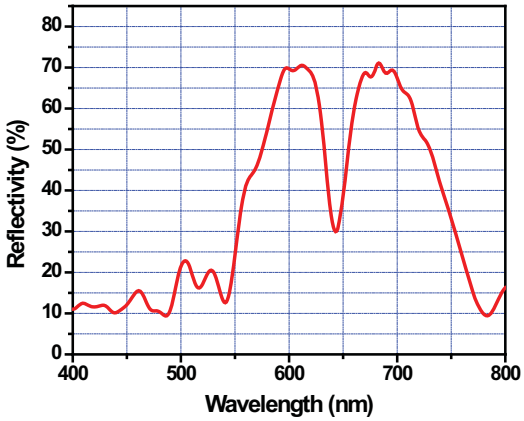

Fig. 25. Reflection spectrum of PS micro-cavity with transmission band of 650nm made by spacer of λ/2- thickness sandwiched between 5-period DBR.

For a prevention of ageing process of PS layers we used thermal annealing process of PS samples to obtain SRSO materials. The thermal annealing process used for SRSO has four steps: i) first the PS samples were kept at 60^0C for 60 min in air ambient to stabilize the PS

structures; ii) the pre-oxidation of PS samples was performed at 300^0C for different times varying from 20 to 60 min in oxygen ambient; iii) slowly increasing temperature up to 900^0C and keeping samples for 5-10 min in oxygen ambient iv) keeping the samples in Nitrogen atmosphere at temperature of 900-1000^0C for 30 min and then the temperature was decreased with very slow rate to room temperature. Table 5 presents the shift of transmission band in the spectra of Fabry-Perot filters based on the as-prepared and thermally annealed PS micro-cavity at 300^0C and 900^0C in oxygen ambient, respectively.

Samples	Centered wavelength of transmission (nm)	Line-width of transmission (nm)	Distinction ratio (%)
as-prepared sample	643.9	22.2	40
300^0/40 min	565.6	22.6	34
300^0/40 min + 900^0C/5 min	472.5	19.2	25

Table 5. Shift of narrow transmission band in the spectra of Fabry-Perot PS filters (the anodization condition was shown in table 4)

The 900^0C oxidation decreases the centered wavelength of transmission by more than 170nm and the reflective distinction ratio on 15%, while the line-width of transmission does not change. This can be explained as follows: the centered wavelength of transmission corresponds to the optical thickness of spacer layer that is the product of refractive index and layer thickness. During the oxidization process at high temperature the layer thickness and refractive index of spacer decreased, which causes the shift of transmission wavelength and decrease of reflective distinction ratio of micro-cavity.

6. Conclusions

We have demonstrated the electrochemical method combined with thermal annealing for making PS and SRSO layers. The advantages of electrochemical method compared with others to fabricate PS and SRSO layers are: low-cost fabrication and experimental setup; compatibility to silicon technology for optoelectronic devices; fast fabrication process and easily varying refractive index over wide range.

We showed that the ageing of PS by natural oxidation is disturbing as well as it causes a change of the emission wavelength of nc-Si, refractive index of PS layers by the change of Si nano-particle sizes. The experimental results indicate that the intense and stable emission in the blue zone of the PL spectra observed in the considered PS samples relates to defects in silicon oxide layers. For prevention of natural oxidation of PS layers we used thermal annealing to obtain SRSO layers, which have more stable optical properties in operations. Also, the Er-doped SRSO multi-layers with good waveguide quality fabricated by using the electrochemical method combined with thermal annealing are presented. The influence of the parameters of the preparation process, such as the resistivity of Si-substrate, the HF concentration, the drift current density, and the oxidation temperature, on the optical properties of the Er-doped SRSO waveguides was studied and discussed in detail. The luminescence emission of Er ions in the SRSO layers at 1540 nm was strongly increased in comparison with that of Er-doped silica thin film. The evidence for energy transfer between nc-Si and Er ions in Er-doped SRSO layer was obtained by changing the excitation wavelength.

Finally, we have demonstrated the electrochemical process for making interference filters and DBR micro-cavity based on PS and SRSO multi-layers with periodical change of refractive indices of the layer stacks. For the optimal parameters of interference filters and micro-cavities based on PS and SRSO multi-layers, we use Transfer Matrix Method for simulation of reflectivity and transmission of interference filters and DBR micro-cavity with the data obtained from experiments. We successfully fabricated the interference filters and DBR micro-cavity based on porous silicon multilayer which has the selectivity of wavelength in a range from visible to infra-red range with the reflectivity of about 90% and transmission line-width of 20nm. The spectral characteristics of those multi-layers such as desired centered wavelength (λ_0), the FWHM line-width of spectrum, reflectance and transmission wavelength have been controlled. A good correspondence between simulation and experimental results has been received. The imperfection of interfaces of layers created by electrochemical etching was used to explain a deformation of reflective spectrum from filters having few periods. The SRSO thin films with single and multi-layer structures produced by electrochemical method have a big potential for applications in the active waveguide, optical filter, chemical and biosensors, DBR micro-cavity lasers.

7. Acknowledgements

This work was supported in part by the National Program for Basic researches in Natural Science of Vietnam (NAFOSTED) under contract No. 103.06.38.09. A part of the work was done with the help of the National Key Laboratory in Electronic Materials and Devices, Institute of Materials Science, Vietnam Academy of Science and Technology, Vietnam. The author would like to thank Pham Duy Long for his help with Autolab equipment.

8. References

Amato, G., Rosenbauer, M. (1997). Absorption and photoluminescence in porous silicon, in Amato et al. (ed.), *Structure and Optical Properties of Porous Silicon Nanostructures*, Gorden and Breach Science Publishers, Amsterdam, 3-52

Anderson, M.A., Tinsley-Brown, A., Allcock, P., Perkins, E.A., Snow, P., Hollings, M., Smith, R.G., Reeves, C., Squirrell, D.J., Nicklin, S., Cox, T.I. (2003), Sensitivity of the optical properties of porous silicon layers to the refractive index of liquid in the pores, *Phys. Stat. Sol. (a) 197*, 528-533

Barla, K., Herino, R., Bomchil, G. (1986). Stress in oxidized porous silicon layers, *J. Appl. Phys. 59*, 439-441

Bettotti, P., Cazzanelli, M., Dal Negro, L., Danese, B., Gaburro, Z., Oton, C.J., Vijaya Prakash, G., Pavesi, L. (2002). Silicon nanostructure for photonics, *J. Phys.: Condens. Matter. 14*, 8253- 8281

Bui Huy, Pham Van Hoi, Phan Hong Khoi, Nguyen Thuy Van, Do Thuy Chi (2011). Porous silicon as a promising material for photonics, *Int. J.NanoTech. 8*, 360-370

Bui Huy, Phi Hoa Binh, Bui Quang Diep, Phi Van Luong (2003). Effect of ageing on the luminescence intensity and lifetime of porous silicon: role of recombination centers, *Physica E 17*, 134-136

Bui Huy, Pham Van Hoi, Phi Hoa Binh, Tran Thi Kim Chi, Le Quang Huy, Nguyen Quang Liem (2006). Effect of ageing on the statically and time-resolved photoluminescence spectra of porous silicon, *J. Phys. IV France 132*, 321-324

Calcott, P.D.J., Nash, K.J., Canham, L.T., Kane, M.J., Brumhead, D. (1993) Spectroscopic identification of the luminescence mechanism of highly porous silicon, *J. Lumines. 57*, 257-269

Canham, L.T. (1990). Si quantum wire arrays fabrication by electrochemical and chemical dissolution of wafer, *Appl. Phys. Lett.57,* 1046-1048

De Stefano, L., Rendina, I., Moretti, L., Rossi, A.M. (2003), Optical sensing of flammable substances using porous silicon microcavities, *J. Mater. Sci. and Eng. B100*, 271-274

Elhouichet, H., Oueslati, M. (2007). Rare earth ions in porous silicon: optical properties, *J. Phys. Stat.Sol. (a), 204*, No.5, 1497-1501

Friolo, F., Franzo, G., Pacifici, D., Vinciguerra, V., Iacona, F., Irrena, A. (2001). Role of the energy transfer in the optical properties of undoped and Er-doped interacting Si nanocrystals, *J. Appl. Phys. 89*, 264-272

Frohnhoff, S., Berger, M.G., Thönissen, M., Dicker, C., Vescan, L., Munder, H., Lüth, H. (1995). Formation techniques for porous silicon superlattices, *Thin Solid Films 255*, 59-62

Gao, T., Gao, J., Sailor, M.J. (2002), Tuning the response and stability of thin film mesoporous silicon vapor sensors by surface modification, *J. Langmuir 18*, 9953-9957

Gorelkinskii, Yu.V., Abdullin, Kh.A., Kalykova, G.K., Kikarin, S.M., Mukashev, B.N. (2008). Stable ultraviolet photoluminescence of nanoporous silicon, *J. Mater.Sci. & Eng.B 147*, 258-261

Herino, R., Bomchil, G., Barla, K., Bertrant, C., Ginoux, J.L. (1987), Porosity and Pore size distributions of Porous silicon layers, *J. Electrochem. Soc. 134*, 1994-2000

Huy. B., Cham T.T., Vinh H.X., Van D.K. and Hoi P.V. (2008). Erbium-doped silicon-rich oxide waveguides fabricated by using an electro-chemical method, *J. Korean Phys. Soc.53*, 1397-1400

Kanemitsu, Y., Uto, H., Masumoto, Y., Futagi, T., Mimura, H. (1993). Microstructure and optical properties of free-standing porous silicon films: Size dependence of absorption spectra in Si nanometer-sized crystallites, *Phys. Rev. B 48*, 2827-2830

Kimura, T., Yokoi, A., Horiguchi, H., Saito, R., Ikoma, T., Saito, A. (1994). Electrochemical Er-doping of porous silicon and its room-temperature luminescence at 1.54 μm, *Appl. Phys. Lett. 65*, 983-985

Kit, P.G., Polman, A. (2000). Exciton-erbium interactions in Si nanocrystal-doped SiO_2, *J. Appl. Phys. 88*, 1992 (7 page)

Kovalev, D., Averboukh, B., Benchorin, M., Koch, F., Efros, Al.L., Rosen, M. (1996). Optically induced polarization anisotropy in porous silicon, *Phys. Rev. Lett. 77*, 2089-2092

Krüger, M., Hilbrich, S., Thönissen, M., Scheyen, D., Theiβ, W., Lüth, H. (1998). Suppression of ageing effect in porous silicon interference filters, *Opt. Comm. 146*, 309-315

Lehmann, V., Gösele, U. (1991). Porous silicon formation – a quantum wire effect, *Apll. Phys. Lett. 58*, 856-858

Loni, A., Canham, L.T., Berger, M.G., Arens-Fischer, R., Munder, H., Lüth, H., Arrand, H.F., Benson, T.M. (1996), Porous silicon multilayer optical waveguides, *Thin Solid Films 276*, 143-146

Mazzoleni, C., Pavesi, L. (1995). Application to optical components of dielectric porous silicon multilayer, *Appl. Phys. Lett. 67*, 2983-2985

Najar, A., Charrier, J., Ajlani, H., Lorrain, N., Elhouichet, H., Oueslati, M., Haji, L. (2006). Optical properties of erbium-doped porous silicon waveguides, *J. Lumines. 121*, 245-248

Saleh, B.E.A., Teich, M.C. (2007), *Fundamentals of Photonics*, 2nd Edition, Chapter 7, John Wiley&Son, Inc., NewYork.

Shin, J. H., van d'Hoven, G. N., Polman, A. (1995). Origin of the 1.54 μm luminescence of Erbium-implanted porous silicon, *Appl. Phys.Lett. 66*, 2379-2381

Smith, R.L., Collins, S.D. (1992). Porous silicon formation mechanism, *J. Appl.Phys. 71(8)*, R1 (21 pages)

Valance, A. (1997). Theoretical model for early stages of porous silicon formation from n- and p-type silicon substrates, *Phys. Rev. B 55*, 9706-9715

Vincent, G. (1994). Optical properties of porous silicon superlattices, *Appl. Phys. Lett. 64*, 2367 (3 page)

Volk, J., Balazs, J., Tóth, A.L., Bársony, I. (2004), Porous silicon multilayers for sensing by tunable IR-transmission filtering, *J. Sensors & Actuators B100,* 163 -167

Weiss, S.M., Fauchet, P.M. (2003), Electrical tunable porous silicon active mirrors, *Phys. Stat. Sol (a) 2*, 556-560

Wolkin, M.V., Jorne, J., Fauchet, P.M. (1999). Electronic states and luminescence in porous silicon quantum-dots: the role of oxygen. *Phys. Rev. Lett. 82*,197-200

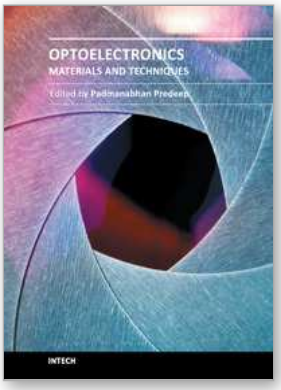

Optoelectronics - Materials and Techniques

Edited by Prof. P. Predeep

ISBN 978-953-307-276-0
Hard cover, 484 pages
Publisher InTech
Published online 26, September, 2011
Published in print edition September, 2011

Optoelectronics - Materials and Techniques is the first part of an edited anthology on the multifaceted areas of optoelectronics by a selected group of authors including promising novices to the experts in the field. Photonics and optoelectronics are making an impact multiple times the semiconductor revolution made on the quality of our life. In telecommunication, entertainment devices, computational techniques, clean energy harvesting, medical instrumentation, materials and device characterization and scores of other areas of R&D the science of optics and electronics get coupled by fine technology advances to make incredibly large strides. The technology of light has advanced to a stage where disciplines sans boundaries are finding it indispensable. Smart materials and devices are fast emerging and being tested and applications developed in an unimaginable pace and speed. Here has been made an attempt to capture some of the materials and techniques and underlying physical and technical phenomena that make such developments possible through some real time players in the field contributing their work and this is sure to make this collection of essays extremely useful to students and other stake holders such as researchers and materials scientists in the area of optoelectronics.

INTECH
open science | open minds

InTech Europe
University Campus STeP Ri
Slavka Krautzeka 83/A
51000 Rijeka, Croatia
Phone: +385 (51) 770 447
Fax: +385 (51) 686 166
www.intechopen.com

InTech China
Unit 405, Office Block, Hotel Equatorial Shanghai
No.65, Yan An Road (West), Shanghai, 200040, China
中国上海市延安西路65号上海国际贵都大饭店办公楼405单元
Phone: +86-21-62489820
Fax: +86-21-62489821